Modeling and Simulation of a Parametrically Resonant Micromirror With Duty-Cycled Excitation

Wajiha Shahid, Zhen Qiu, Xiyu Duan, Haijun Li, Thomas D. Wang, and Kenn R. Oldham

***Abstract*— High frequency large scanning angle electrostatically actuated microelectromechanical systems (MEMS) mirrors are used in a variety of applications involving fast optical scanning. A 1-D parametrically resonant torsional micromirror for use in biomedical imaging is analyzed here with respect to operation by duty-cycled square waves. Duty-cycled square wave excitation can have significant advantages for practical mirror regulation and/or control. The mirror's nonlinear dynamics under such excitation is analyzed in a Hill's equation form. This form is used to predict stability regions (the voltage-frequency relationship) of parametric resonance behavior over large scanning angles using iterative approximations for nonlinear capacitance behavior of the mirror. Numerical simulations are also performed to obtain the mirror's frequency response over several voltages for various duty cycles. Frequency sweeps, stability results, and duty cycle trends from both analytical and simulation methods are compared with experimental results. Both analytical models and simulations show good agreement with experimental results over the range of duty cycled excitations tested. This paper discusses the implications of changing amplitude and phase with duty cycle for robust open-loop operation and future closed-loop operating strategies. [2013-0400]**

***Index Terms*— MEMS, micro-mirror, parametric resonance, Hill's equation, nonlinear dynamics.**

I. Introduction

THE GOAL of this work is to characterize, in terms of mathematical analysis, simulation, and experimentation, the behavior of a parametrically-resonated micro-mirror subject to duty-cycled square wave excitations. Parametric resonance was first observed in 1831 by Faraday in surface waves in a fluid-filled cylinder under vertical excitation [1], and has since been explored in many branches of engineering and physics. Examples of parametric resonance have been observed in roll of ships [3]–[5], bridges [6], [7] and even in biological systems [8]. Parametric resonance is used widely in MEMS applications, for sensing using micro-cantilevers [9], improving rate resolution in MEMS gyroscopes [10], and amplifying motion of resonators [11], tuning filters [12] and laser scanning display systems [13]. Parametric amplifiers have also been employed in medicine for amplification and transmission of magnetic resonance signals [14].

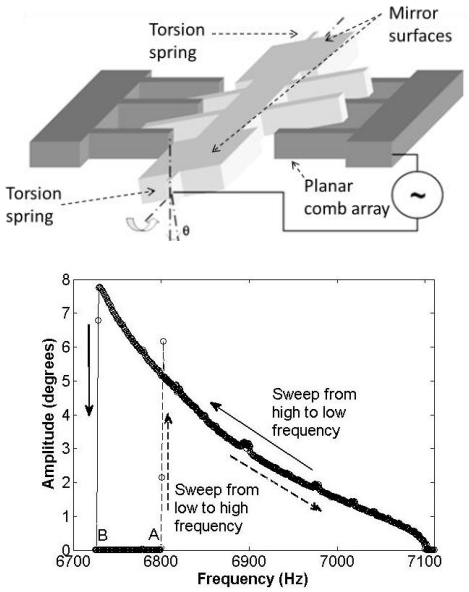

Fig. 1. (Top) Key components of the rectangular 1D micro-mirror (Bottom) Experimentally obtained frequency response of the micro-mirror at 40V and 50% duty cycle. Point 'A' illustrates the frequency at which the mirror begins its oscillations and Point 'B' illustrates the frequency at which the mirror achieves its maximum scanning amplitude.

Meanwhile, the use of MEMS micro-mirrors for biomedical imaging has gained popularity and several groups [15]–[17], [37], [42], have explored this application extensively. The 1D parametrically-resonant, electrostatically-actuated torsional MEMS micro-mirror presented in this paper is to be used for dual axes confocal or multi-photon microscopy [18], [44]. A schematic image of the micro-mirror and its sample frequency response is shown in Fig. 1, while a scanning electron microscope image of a completed mirror is shown in Fig. 2. Its large tilting angles can be advantageous for endoscopic imaging, providing a large field of view from simpler fabrication processes [19], [43] than previously demonstrated micromirrors for dual-axes confocal microscopy that did not utilize parametric resonance.

Despite substantial study of a variety of MEMS structures oscillating under parametric resonance, there have been few reported results for parametric resonant behavior under square wave rather than resonant behavior. This is in spite of the

Manuscript received December 27, 2013; revised March 4, 2014; accepted March 20, 2014. Date of publication April 21, 2014; date of current version November 25, 2014. Subject Editor O. Solgaard.

W. Shahid and K. R. Oldham are with the Mechanical Engineering Department, University of Michigan, Ann Arbor, MI 48105 USA (e-mail: wshah@umich.edu; oldham@umich.edu).

Z. Qiu and X. Duan are with the Department of Biomedical Engineering, University of Michigan, Ann Arbor, MI 48109 USA (e-mail: zqiu@umich.edu; dxy@umich.edu).

H. Li is with the Department of Internal Medicine-Gastroenterology Division, University of Michigan, Ann Arbor, MI 48109 USA (e-mail: haijunl@umich.edu).

T. D. Wang is with the Department of Biomedical Engineering, Department of Internal Medicine-Gastroenterology Division, University of Michigan, Ann Arbor, MI 48109 USA (e-mail: thomaswa@umich.edu).

Color versions of one or more of the figures in this paper are available online at http://ieeexplore.ieee.org.

Digital Object Identifier 10.1109/JMEMS.2014.2315518

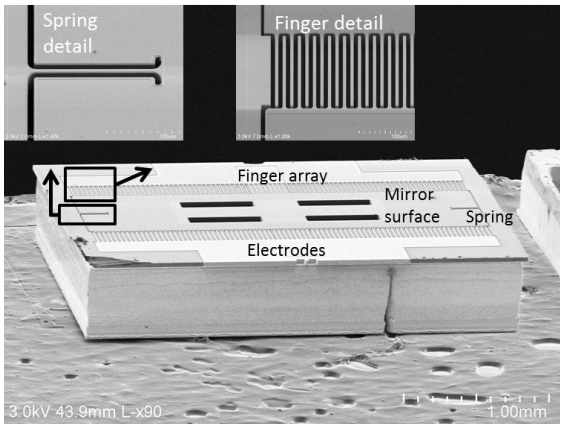

Fig. 2. Scanning electron microscope image of a parametrically-excited micro-mirror of the type used for testing, with detail of torsion hinge spring and electrostatic comb finger array.

experience of various researchers that in applying square wave excitations to a system to cause parametric resonance, the duty cycle can regulate behavior and affect stability regions [18]. Most notably, Ataman et al introduced experimental results for a parametrically resonant MEMS micro-mirror driven by a square wave at 50% duty cycle in comparison with outcomes from sinusoidal excitation [28]. More recently, Maruyama et al proposed a new scheme of scanning amplitude control using the duty ratio of pulse width modulation of voltage for a non-parametrically resonant optical micro-scanner [18], [29].

Duty-cycled mirror operation has several possible advantages. Though not all of these advantages can necessarily be utilized at the same time, they include:

1) A capacitive load at a fixed voltage can be driven much more efficiently and with much less expensive hardware by pulse-width modulation than by an analog waveform.
2) Under switched operation, duty cycles other than 50% may result in greater robustness to system variation.
3) In closed-loop operation, control of duty cycle provides a method for tuning amplitude or phase without use of additional voltage levels.
4) In imaging that uses multiple axes, typically via Lissajous scanning, specific frequency and phase combinations can provide more efficient image acquisition than others. Availability of both voltage and duty cycle can allow frequency and phase to be tuned independently over certain operating ranges.

This work describes analysis procedures for the 1D parametrically resonant mirror that supports the potential advantages above. For basic operation under various duty cycles (points 1 and 2) the stability regions for parametric resonance are found analytically and by simulation. For future phase control with feedback (points 3 and 4) sample phase behavior as a function of duty cycle and frequency is obtained.

To perform this analysis, the paper initially adapts the analytical Hill's Equation approach to include varying duty cycles. A secondary improvement to analytical modeling is a proposed method to account for large deflection under highly nonlinear capacitance behavior. Complicated capacitance models are common for parametrically resonant micro-actuators, and this has typically limited the amplitudes over which analytical stability or, especially, amplitude models are accurate. For example, parametric resonance results by Ataman et al. for out-of-plane mirror oscillation could only be closely fit in the linear region of a polynomial capacitance description [28]. Rhoads et al. extended systematic scanning results to third order polynomial forcing [38], but this cannot describe the full operating range of the current device. Linzon et al. used a capacitance model based on hyberbolic sine functions to make predictions over larger deflections of a parametrically resonant cantilever, but amplitude agreement was still only within approximately 50% of experimental values, and again only for sinusoidal operation [39].

This work takes advantage of comparative simplicity of square wave driving voltages to create an approximation of mirror-deflection from a non-parametric model, which can be iterated with the Hill's equation stability analysis to produce large angle amplitude and stability predictions. This is found to give very close agreement over a wide range of displacements with respect to stability predictions, and better amplitude predictions than previous works at large deflections, though accuracy is still comparatively limited. Analytical solutions are complemented by simulation of the micro-mirror response to identify trends in micro-mirror operation under duty-cycled operation, and identify other possible contributions to differences between experimental and model results.

II. Analytical Modeling

Parametrically resonant systems exhibit large amplitudes for a small parametric excitation when they are driven at frequencies near $2w_0/n$, where w_0 is the natural frequency of the system and n is an integer ≥ 1 [18], [20], [21]. These systems are governed by homogenous differential equations with rapidly varying, typically periodic coefficients [18], [21]. In many applications, the equations of motion governing a parametrically excited system can be simplified to take the form of a Hill's equation [22]. This is a class of homogeneous, linear, second- order differential equations with real periodic coefficients [22], [23]. Floquet theory [23] is typically used to discuss the stability of periodic solutions for such periodic systems; however, this method requires a large number of numerical integrations that can limit its use, especially if the coefficients of the equations depend on certain parameters [22], [24]. There is a large body of literature that examines the stability and dynamics of Hill's type equations in parametric resonance [25]–[27].

The 1D micro-mirror presented in this paper operates in its torsional mode [18], [19], [22]. Frequency point 'A' on the sample frequency response in Fig. 1 indicates the frequency at which the mirror begins oscillating during an upward frequency sweep and illustrates how the scanning angle decreases as the mirror frequency is swept higher from 'A'. *Upward sweep* or *up-sweep* simply refers to a frequency sweep from a low frequency to a high frequency in the frequency spectrum. Point 'B' on the frequency plot indicates the frequency corresponding to the maximum scan amplitude, reached by a downward sweep. *Downward sweep* or *down-sweep* simply

$$V(t) = A\left(\sqrt{\left[\sigma + \sum_{m=1}^{\infty}\left(\frac{1}{m\pi}\sin(2\pi m\sigma)\right)\cos(wmt) + \frac{1}{m\pi}(1-\cos(2m\pi\sigma))\sin(wmt)\right]}\right). \quad (3)$$

refers to a frequency sweep from a high frequency to a low frequency in the frequency spectrum. Since perturbing the frequency at Point 'B' could result in the mirror oscillations coming to a complete halt, feedback control strategies, as would be supported by analysis in the final section of this paper, are useful to ensure that the maximum scanning angle is maintained just above Point 'B'.

A. System Model

The equation of motion of the single DOF parametrically resonant MEMS micro-mirror is governed by [20]:

$$J\ddot{\theta} + c\dot{\theta} + k\theta = F(t,\theta) \quad (1)$$

where θ is the rotation angle of the mirror, J is the mass moment of inertia of the mirror, k is the torsional spring stiffness constant, c is the average damping constant and F is the applied torque. The out of plane torsional mode was the dominant vibration mode of the mirror and modal analysis in ANSYS confirmed that the resonant frequencies of other modes were well separated from the torsional mode frequency. The damping constant and spring stiffness constant were assumed constant for the purpose of this analysis. The applied torque, F, is defined as

$$F(t,\theta) = N\frac{1}{2}\frac{dC}{d\theta}V^2(t) \quad (2)$$

where N is the number of comb fingers on one mirror side and $dc/d\theta$ is the rate of change of capacitance for one comb finger with respect to angular displacement. $V(t)$ is the periodic square wave driving signal and it assumes the form as a Fourier series, as shown in (3) at the top of this page.

In (3), σ is the duty cycle fraction, A is the amplitude of the input excitation signal, w is the frequency, t represents time and m is a non-zero integer. Equation (3) was obtained by expressing the following periodic function in Fourier series in terms of the duty cycle, for $k = 0, 1, 2, \ldots$,

$$V(t) = \begin{cases} A, & kT < t < kT + \sigma T \\ 0, & kT + \sigma T < t < (k+1)T \end{cases} \quad (4)$$

where T is the time period for one cycle. Using a square root voltage representation in (3) isolates parametric effects from the harmonic effects [30]. This form has been used extensively in literature for studying nonlinear Mathieu equations and Duffing equations [31], [32].

B. Stability Analysis

For stability analysis, the forcing function as defined by (2) is linearized to define a constant, a, such that $dC/d\theta \approx -a\theta$. The process for defining a capacitance model, $C(\theta)$, and selecting a is described in the Section II.C. Given a value of a, and introducing dimensionless constant, $\tau = wt/2$, (1) becomes:

$$\frac{d^2\theta}{d\tau^2} + \frac{2c}{Jw}\frac{d\theta}{d\tau} + \left(\frac{4k}{Jw^2} + \frac{4}{Jw^2}aV^2(\tau)\right)\theta = 0 \quad (5)$$

Isolating amplitude term, A^2

$$\frac{d^2\theta}{d\tau^2} + \frac{2c}{Jw}\frac{d\theta}{d\tau} + \left(\frac{4k}{Jw^2} + \frac{4}{Jw^2}aA^2\left[\sigma + \left(\sum_{m=1}^{\infty}\left(\frac{1}{m\pi}\sin(2\pi m\sigma)\left(\cos(2m\tau) + \frac{1}{m\pi}(1-\cos(2m\pi\sigma))\sin(2m\tau)\right)\right)\right)\right]\right)\theta = 0 \quad (6)$$

and defining

$$\mu = \frac{c}{Jw} \qquad \delta = \frac{4[k+\sigma A^2 a]}{Jw^2} \qquad \varepsilon = \frac{4}{Jw^2}aA^2 \quad (7)$$

results in a form of the damped Hill's equation for parametrically excited systems [21] such that,

$$\frac{d^2\theta}{d\tau^2} + 2\mu\frac{d\theta}{d\tau} + [\delta + \varepsilon f(\tau)]\theta = 0 \quad (8)$$

where

$$f(\tau) = \sum_{m=1}^{\infty}\alpha_m\cos(2m\tau) + \beta_m\sin(2m\tau) \quad (9)$$

$$\alpha_m = \frac{1}{m\pi}\sin(2m\pi\sigma), \quad \beta_m = \frac{1}{m\pi}(1 - cos(2m\pi\sigma)) \quad (10)$$

Here, (8) is in a standard form from which the frequency bounds of stable oscillations with respect to applied voltage, A, and duty cycle, σ can be determined. This analysis is performed using the Lindstedt Poincare technique [33], as described in Appendix I. The outcome of this analysis is to produce critical values of the dimensionless constant δ at which the system transitions from stable to unstable regions,

$$\delta = n^2 \pm \frac{1}{2}\sqrt{\left(\beta_m^2 + \alpha_m^2\right)\varepsilon^2 - 16n^2\mu^2}\ldots \quad \ldots. \quad (11)$$

where α_m and β_m are coefficients from the Lindstedt-Poincare analysis, and the equations of the boundary curves in the frequency – voltage amplitude domain can be obtained for parametric resonance at $n = 1, 2, 3\ldots.$ by replacing (11) into the definition of δ from (7).

C. Capacitance Model

To predict behavior of a specific MEMS mirror using the preceding analysis, a critical need is to accurately define the nonlinear capacitance of the mirror versus angular displacement. In addition, as the analysis in Section II.B relies on a linearized version of that capacitance model, the linearization must be done in an appropriate manner. While incorporating nonlinear capacitance directly into the analysis would be an

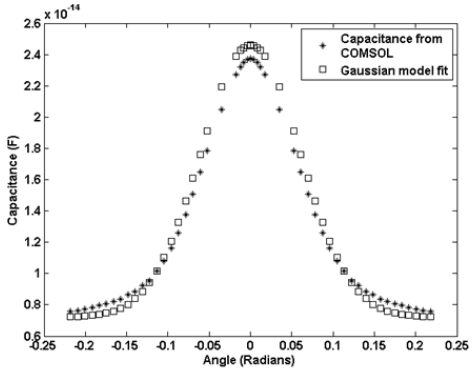

Fig. 3. Gaussian model fit to the capacitance extracted from COMSOL.

alternate approach, it will be shown that selecting an appropriate range for averaging the derivative of capacitance produces good agreement with experimental results, with direct solution with nonlinear $C(\theta)$ future work.

First, capacitance of the mirror's fixed comb-drive and a pair of movable comb-drives was modeled in COMSOL Multiphysics software to capture the fringe capacitance effects. The movable comb drive was rotated about the torsional axis of the mirror to obtain the capacitance corresponding to each angle and the following model, referred to as a Gaussian function due to its typical use for describing normal probabilities, was used as the best fit for the capacitance-angle relationship:

$$C = de^{-\frac{\theta^2}{b}} + h \tag{12}$$

where C is the capacitance, θ is the mechanical scanning amplitude and d, b, h are constants and $h = 7.21\text{E-}15\ F$. Fig. 3 illustrates the capacitance model from COMSOL and its respective Gaussian fit, though some experimental tuning was done to account for fabrication variance, described in Section III. Previously, stability curves for parametrically-resonated micro-actuators have been derived using a polynomial capacitance fit [22], but this approach failed to provide a sufficiently accurate description of the 'tails' of a capacitance motion when large angle motion was generated in this current study.

To select a for a given excitation amplitude and duty cycle, given the wide range of angular displacements experienced and the underlying capacitance, an iterative process was used:

1) First, for a given excitation frequency, an initial prediction of scanning amplitude, $\theta_{nominal}$, and a corresponding operational voltage, $V_{nominal}$, was made.
2) Next, $\theta_{nominal}$ and $V_{nominal}$ were used to compute an average applied force $\bar{F}(\theta_{nominal}, \sigma, \hat{\phi})$ as if the mirror were being operated non-parametrically under differential capacitance, using an approximation of the binary square wave input, as described below, with $\hat{\phi}$ an estimated phase angle for the system. This force estimation is discussed in more detail in Section II.D. Then, (1) was solved numerically to obtain the approximate mechanical scanning angle, θ, at $V_{nominal}$.
3) Steps 1 and 2 were iterated until convergence was obtained such that $\theta_{nominal} = \theta$. In other words, the torque provided at a given voltage was appropriate to the amplitude that would be obtained non-parametrically.
4) Using the predicted amplitude θ from Step 3, a was estimated as the best linear fit of $dC/d\theta - \theta$ to θ from (12). (For small rotations about the stable equilibrium, this step could be neglected, with the small displacement a for the capacitance curve, $dC/d\theta$, taken as the linear fit of (12) at $\theta = 0$, and this was accurate for scanning amplitudes ranging from about $-3°$ to $+3°$.
5) The selected value of a from Step 4 was used to tabulate the voltage, $V_{critical}$, using (7) and (11), corresponding to the stability limit at a given frequency using the analysis from Section II.B.
6) Steps 1 to 5 were iterated until $V_{nominal}$ from the analytical amplitude calculations and $V_{critical}$ from the Hill's equation analysis converged to the same voltage for a given frequency of excitation. In other words, this ensured that the assumed amplitude used for capacitance modeling in the stability analysis was consistent with reasonable amplitude oscillations of the system at that frequency. Further discussion on why such an approximation appears to be effective is given in Section V.

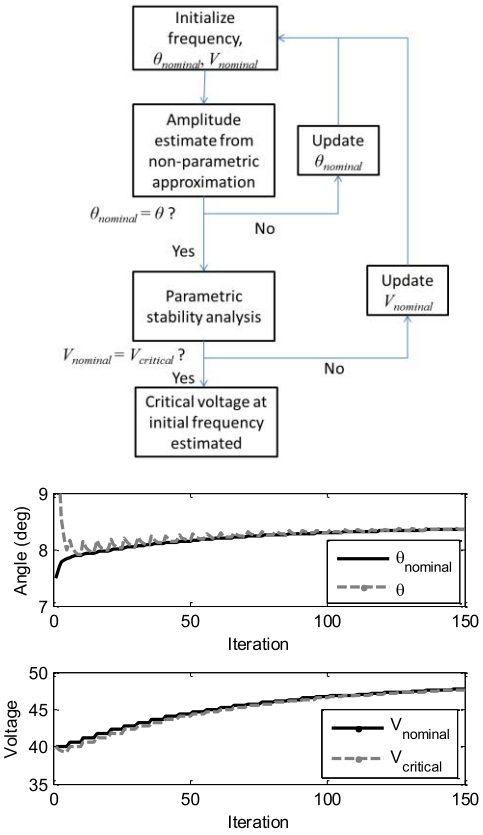

Fig. 4. Non-linear capacitance approximation for parametric stability analysis uses an iterative process (top) of non-parametric amplitude approximation and parametric stability bound calculations, until amplitude and voltage levels are in agreement, as in the sample solution (bottom) showing convergence of angle and voltage, in this case to a stability bound of 48 V at 6830 Hz for 50% duty cycle.

Fig. 4 shows the analysis process in a flow chart format, as well as sample convergence of $V_{nominal}$ and $V_{critical}$ for 50%

duty cycle at 6830 Hz, with an initial stability bound estimate at 40 V being updated to a final stability bound of 48 V for the selected duty cycle and frequency. Additional duty cycles and frequencies are selected to obtain other critical voltage in voltage-frequency stability curves (results in Section V.B). Each such analysis requires less computation time than full numerical simulation at a single frequency, for time discretization short enough to capture the parametric phenomenon.

D. Differentially-Driven Amplitude Approximation

The approximation of the forcing function in Step 2 in Section II.C is obtained by casting the periodic signal in (4) as a differential input, $\hat{V}$, over two time periods, or

$$\hat{V}(t) = \begin{cases} A, & (2k-1)T \le t < (2k-1)T + \sigma T \\ 0, & (2k-1)T + \sigma T \le t < 2kT \\ -A, & 2kT \le t < 2kT + \sigma T \\ 0, & 2kT + \sigma T \le t < (2k+1)T \end{cases}$$
$$= \hat{f}(t) = \sum\nolimits_{m=1}^{\infty} \hat{\alpha}_m \cos\left(\frac{w}{2}mt\right) + \hat{\beta}_m \sin\left(\frac{w}{2}mt\right) \quad (13)$$

where $\hat{f}(t)$, $\hat{\alpha}_m$, and $\hat{\beta}_m$ are the differential representation of the periodic input and its Fourier expansion having twice the period of the original driving signal.

The amplitude of the system is then estimated by solving

$$J\ddot{\theta} + c\dot{\theta} + k\theta = \hat{f}(t)\bar{F}(\theta_{nominal}, \sigma, \hat{\phi}) \quad (14)$$

where $\bar{F}(\theta_{nominal}, \sigma, \hat{\phi})$ is an estimated average force taken from the average angle of a hypothesized motion, $\hat{\theta}(t)$, while the input is in its 'on' state, i.e. between 0 and σT, hypothesized as

$$\hat{\theta}(t) = \theta_{nominal}\cos\left(\frac{w}{2}t + \hat{\phi}\right). \quad (15)$$

The anticipated phase angle of the response, $\hat{\phi}$, as measured from the rising edge of the excitation signal, is estimated by the delay implied by the Fourier expansion in (13) and the phase angle of the system (14) at the excitation frequency, or

$$\hat{\phi} = \text{atan}\left(\frac{\hat{\beta}_1}{\hat{\alpha}_1}\right) + \angle G\left(\frac{jw}{2}\right) + \pi \quad (16)$$

where $\hat{\alpha}_1$ and $\hat{\beta}_1$ are the first two coefficients in the Fourier expansion of the differential approximation of the driving force in (13) and $G(jw)$ is the transfer function of the linearized system in (14). A factor of π in (16) accounts for the change in phase in polarity from the purely attractive parametric excitation to the differential approximation. The average driving force in (14) is then finally calculated from

$$\bar{F}\left(\theta_{nominal}, \sigma, \hat{\phi}\right) \approx \begin{cases} F\left(\bar{\theta}_{nominal}\big|_0^{\sigma T}\right) & \sigma T \le t_{switch} \\ F\left(\bar{\theta}_{nominal}\big|_0^{t_{switch}}\right) + F\left(\bar{\theta}_{nominal}\big|_{t_{switch}}^{\sigma T}\right) & t_{switch} < \sigma T \end{cases} \quad (17)$$

with t_{switch} being the time at which the sign of the hypothesized motion $\hat{\theta}(t)$ changes, or

$$t_{switch} = \frac{2}{w}\left(\frac{\pi}{2} - \hat{\phi}\right) \quad (18)$$

TABLE I
MODEL PARAMETERS OF THE MICRO-MIRROR

J (kg.m^2)	k (N.m/rad)	c (N.s.m/rad)	N	d (F)	b (rad^2)
6.15E-15	2.76E-06	1.7E-12	200	1.74E-14	7.20E-3

and $\bar{\theta}_{nominal}$ is the average angle of the mirror over a given time period,

$$\bar{\theta}_{nominal}\big|_{t_1}^{t_2} = \int_{t_1}^{t_2} \theta_{nominal}\cos\left(\frac{w}{2}t + \hat{\phi}\right) dt. \quad (19)$$

Since (19), (16), and thus also (17) can be solved analytically, and amplitude of θ in (14) obtained by Fourier analysis with (13), the above equations provide a rapid method for estimating motion amplitude from the original nonlinear capacitance model (12) during Steps 1-3 of the iterative solution process. This approximation of the mirror forcing takes advantage of comparative insensitivity of stability margins from (11) to precise driving amplitudes to provide excellent predictions of voltage-frequency stability of the mirror, as will be seen in Section V.B. It also provides reasonably accurate amplitude approximations, and good phase predictions, as will be seen in Section V.C.

The amplitude estimation procedure is effective in large part because the square wave driving signal substantially simplifies the moment applied to the mirror as a function of time. However, there remains substantial error in the approximation in (17), and a lesser contribution from (16), which can still cause some loss in amplitude accuracy. In addition, the procedure can only be used in conjunction with a stability analysis (Steps 4-6) as it assumes that motion is present to recast the driving force as differential in (13). Reasons for its effectiveness for stability analysis are further discussed in Section V.B., and its capacity for predicting certain robust operating frequencies is shown in Section V.C.

III. SIMULATION AND PARAMETER IDENTIFICATION

Numerical simulations were also used to model micro-mirror behavior. These could also describe nonlinear behavior inherent to this parametrically resonant micro-mirror. In particular, this could further refine amplitude predictions for the mirror. Equation (1) was solved numerically using an Euler scheme to create frequency response curves using the Gaussian capacitance model.

The accuracy of both simulated responses and the analytical stability model depended on obtaining accurate values for the moment of inertia, J, spring constant, k, change in capacitance, $\frac{dC}{d\theta}$, and damping value, c. J and k were tabulated using Finite Element Analysis (FEA) techniques. Modeling k as a large deflection non-linear model in ANSYS FEA confirmed that the spring constant should remain in the linear regime for the range of displacements experimented. $\frac{dC}{d\theta}$ was derived using the capacitance model from COMSOL, as previously described, and c was determined experimentally using the setup described in Section IV.

Table I shows the key design parameters of the micro-mirror taken from the COMSOL model, torsion beam bending

analysis of the mirror flexures, and experimental tests of mirror damping. A frequency spectrum was then simulated for the expected frequency response and the time period were calculated based on the torsional mode frequency (determined using ANSYS). The time step and the simulation end time for each frequency interval were adjusted till they adequately illustrated relevant details of the frequency response, with no further changes from finer time divisions.

Since the vertical comb-drives require a disruption of electrostatic field between the combs for actuation to begin [35], a slight asymmetry between the fixed and movable areas was introduced as an offset angle. To incorporate effects of possible misalignment between the fixed and movable areas stemming from fabrication imperfections, an offset torque in the form of random Gaussian white noise ranging between the order of 10^{-11} and 10^{-10} was added to the forcing function in (1) in the simulation. A square wave generator provided the square wave voltage input within the code.

Since the mirror as fabricated differs slightly in comb finger dimensions and shape from the ideal COMSOL models, parameters b and d from (12) were manually adjusted to provide a best fit for the experimental response for 50% duty cycle and 40 V. b and d were then fixed and used to generate all analytical and simulation results. They vary by 10% for b and 6% in d from values taken directly from COMSOL, and approximately 9% in b and 1% in d from values that would have provided the best fit at 60 V or 30 V. We believe that the reason for different best fit parameters at different voltage levels is that the Gaussian capacitance model still fails to perfectly capture capacitance changes at large angles, though it does handle the variation better than polynomial fits. The final capacitance model used parameters are also given in Table I.

A sample time series during simulation is shown in Fig. 6, showing transient effects during transition from one frequency to another (downsweep from 6920 Hz to 6900 Hz at 50% duty cycle and 40 V). Also shown is a detail of the steady-state response at 6920 Hz, with its normalized input signal.

IV. Experimental Testing

The experimental setup to determine frequency response and damping value is described in this section. The experimental setup to extract frequency response and damping value was identical for micro-mirror dynamics characterization; only the code was altered to extract relevant information for the frequency response and damping experiment. The experimental setup consisted of a data acquisition system (LabVIEW) with a PCI 6115 data acquisition card. This was used to collect data from a position sensing amplifier (OT-301) connected to a laser position sensing detector (On-Trak). The position sensing detector (PSD) was first adjusted to eliminate any offsets and then calibrated. The analog output from LabVIEW was connected to a high voltage amplifier (TEGAM 2350), which was then linked to the 1D micro-mirror to perform frequency sweeping of square wave inputs to the mirror. The mirror was placed on a circuit board mount and the mount was angled at 45° such that the angle between the incident and reflected laser beam was 90°. The laser light source in this setup was a 633 nm Helium Neon laser. Fig. 5 illustrates a schematic of the experimental setup in the laboratory with the laser, micro-mirror and PSD used for frequency response experiments and extraction of phase delay information.

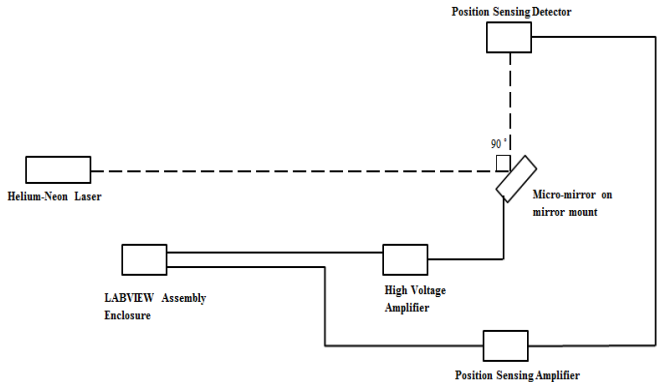

Fig. 5. Schematic of components in the experimental setup to obtain frequency response and damping value. The dotted lines indicate the incident and reflected path of the laser and the solid lines trace connections between the components of the experimental setup.

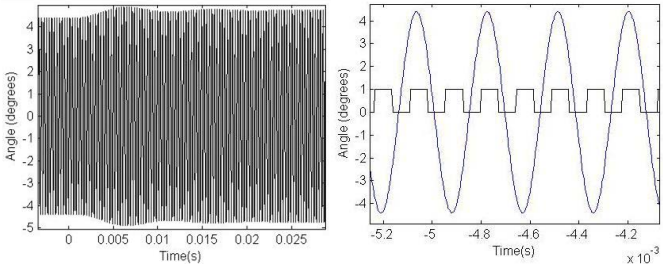

Fig. 6. Sample results from simulation model; (left) down-sweep transition from 6920 Hz to 6900 Hz at 40 V and 50% duty cycle shows transient effects when changing frequency (right) detail during steady-state operation at 6920 Hz shows sinusoidal nature of response and relation to normalized input signal.

V. Results

The following section discusses results for micro-mirror frequency response via numerical simulations and illustrates voltage-frequency charts to characterize stable and unstable regions. All results are for resonance at $n = 1$, where the largest response was obtained from the mirror.

A. Frequency Response

Figs. 7-9 compare experimental and simulated frequency responses of the micro-mirror at 30%, 50%, 60% and 70% duty cycles at 56 V, 40 V and 32 V, respectively. The dashed lines indicate the simulated results for up-sweep and down-sweep cases and the lines with circles indicate the experimentally obtained frequency response. The scanning amplitudes are the mechanical scanning amplitudes.

As can be seen in Figs. 7-9, the frequencies at which the mirror attains maximum amplitude during down-sweep align well with respective frequencies in the experimental data, as do the relative areas of stability and instability under each

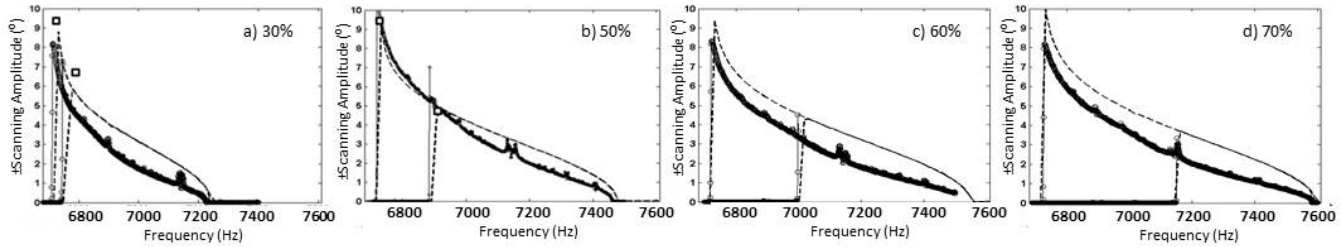

Fig. 7. Simulated outcomes (dotted black lines) at 56V for duty cycles 30% (A), 50% (B), 60% (C) and 70% (D) respectively. Experimental results are indicated using lines with circle markers. Simulated frequencies and amplitudes correspond well with experimental counterparts. Square markers indicate approximate amplitudes used in analytical stability bound generation (Step 2 in Fig. 4).

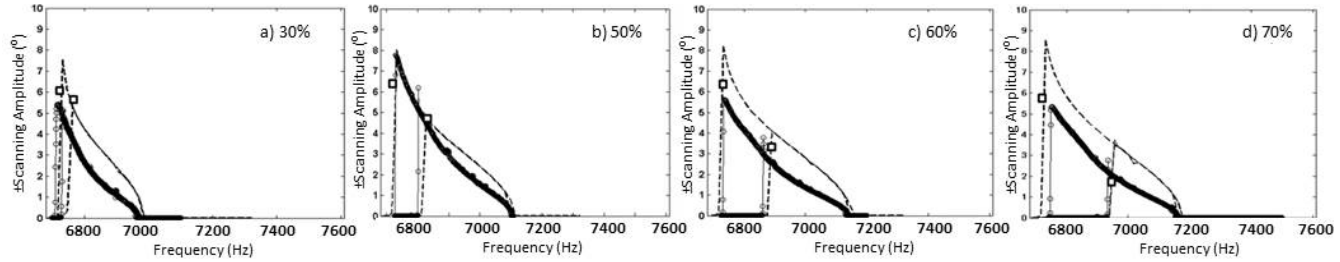

Fig. 8. Simulated outcomes (dotted black lines) at 40V for duty cycles 30% (A), 50% (B), 60% (C) and 70% (D) respectively. Experimental results are indicated using lines with circle markers. Frequencies at which the mirror attains maximum amplitude during up and down sweep align reasonably with respective down-sweep frequencies in the experimental data. Scanning amplitudes predicted by the simulations are higher than the experimentally obtained amplitudes, with the exception of the case at 50% duty cycle. Square markers indicate approximate amplitudes used in analytical stability bound generation (step 2 in Fig. 4).

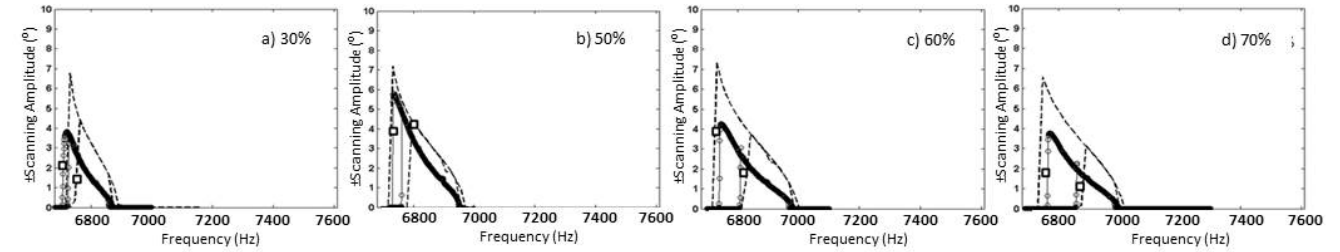

Fig. 9. Voltage – frequency stability regions at 32 V for duty cycles 30% (A), 50% (B), 60% (C) and 70% (D) respectively. The analytical model trend is in good agreement with the experimental results at throughout the voltage range for all duty cycles. Square markers indicate approximate amplitudes used in analytical stability bound generation (step 2 in Fig. 4).

duty cycle. For example, at 30% duty cycle, the relative area of unstable region to stable region is small; however, as duty cycles increase the unstable region progressively increases in size relative to the stable region. Furthermore, even the slight discrepancy in experimental data sometimes observed between up-sweep and down-sweep vibration at the highest frequencies of oscillation (i.e, near 7200 Hz in Fig. 8c or 8d) are observed in simulation.

Amplitude predictions by simulation generally provide a good representation of the shape of amplitude versus frequency, such as the concave-convex curve from the peak as frequency increases. Notably, the shape of the frequency response curve was not captured well by other functional descriptions of the COMSOL capacitance estimates, such as a polynomial fit.

Absolute amplitude predictions are best at higher voltages and lower duty cycles, and there does tend to be a steeper descent from the maximum amplitude in experimental results than predicted by simulation. This discrepancy in frequency response slope appears to be in a large part due to non-ideal square wave generation in experiments, which feature finite rise times and some ripple effects, especially on low-to-high transitions. While a full explanation has yet to be determined analytically, simulation with a low-pass filter inserted into the input voltage to approximate realistic power amplifier response shows steeper slopes for the frequency response from its peak. For example, a rise time of approximately 10% of the excitation frequency leads to an approximately 20% reduction in amplitudes near the low-to-high sweep transition at 40 V, similar to what is seen in the experimental results. The effect is less pronounced for higher voltage simulations, helping explain their better agreement with experimental results. In practice, switching circuit settling time is much longer in the off-state than the on-state, which is consistent with better performance at low duty cycles ($\leq$50%), where the non-ideal decay time is a smaller proportion of the off period.

Another possible source of error is nonlinear damping, as the effective damping coefficient in reality is expected to be slightly higher when fingers are completely overlapping

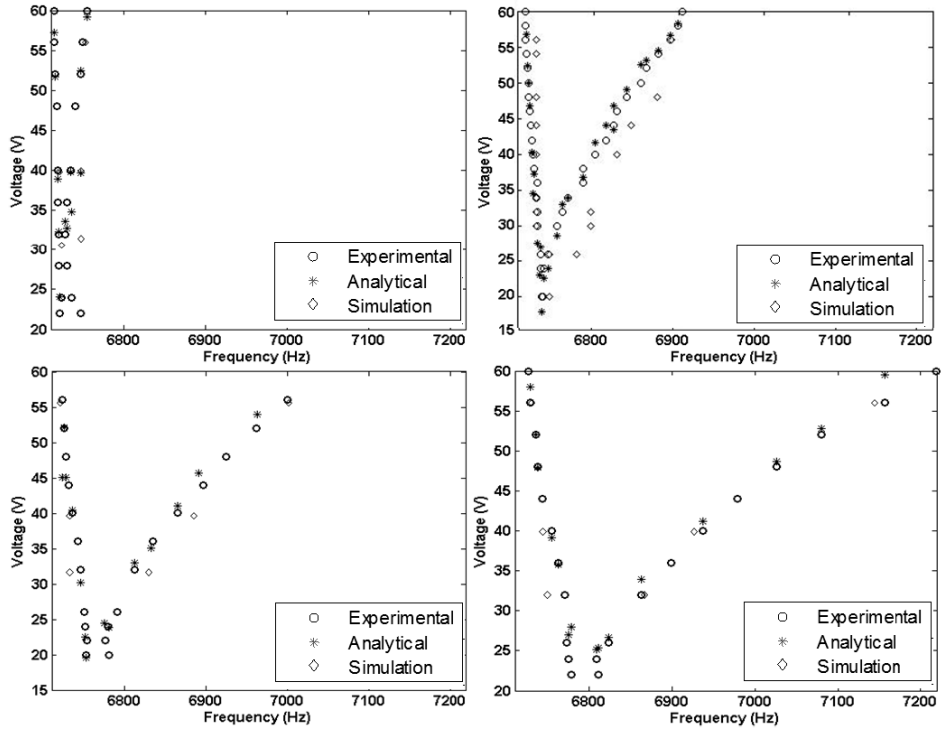

Fig. 10. Critical voltage-frequency combinations for stable up-sweep and down-sweep oscillations are in close agreement by experimental, simulation, and analytical methods for voltages ranging from 20 to 60 V and duty cycles of 30%, 50%, 60%, and 70%, with largest discrepancies at lower voltages during up-sweep operation.

then when they are at large angles. This could also contribute to a larger discrepancies at low voltages and smaller amplitudes, seen in the comparison of experimental and simulation results.

Also shown in Figs. 7-9 are individual amplitude estimates made during stability analysis, during the non-parametric approximation to determine θ in the process shown in Fig. 4. On average, the approximate amplitudes have similar accuracy as simulated results, but there is less consistency to whether they over or underestimate amplitudes. This is likely a consequence of the simplifications made to solve the analytical amplitude, as a single fixed torque on the mirror is used to approximate the capacitive behavior. As will be seen in the following section, exact stability bounds are relatively insensitive to exact motion amplitude, and thus stability analysis tends to work very well even with this level of amplitude estimation error. Likewise, trends across duty cycles are predicted reasonably well, though with some error in absolute amplitude.

B. Voltage - Frequency Stability

While simulation based on the Gaussian capacitance model overall predicts the entire span of the frequency response curves reasonably, the aim of analytical Hill's equation analysis was, first, to verify the effect of assumptions and simplifications employed in analytical derivations in describing the mirror dynamics and, second, to determine how regions of stability and instability change in response to duty cycle variations without resort to time intensive simulation.

Fig. 10 compares predicted and experimental values for the voltage amplitude-frequency stability curves of the micro-mirror tested. The analytical model predicts voltage–frequency stability trends quite accurately in the majority of driving scenarios tested for 30%, 50%, 60% and 70% duty cycle. Again, higher voltages show the best agreement, with very close correspondence to experimental results. As voltage decreased, the analytical model tended to fail to find stability bounds at low voltage ($<$25 V) and higher duty cycles ($>$50%). This suggests that in order to match experimental outcomes at low voltages (20V–24V), the value of a would need to be more precisely know that could be inferred from methods available; the best fit Gaussian model for large amplitude motion is selected to work best for large amplitude motion, and capacitance modeling from COMSOL can be difficult to fit at very small angles due to finite mesh sizing for reasonable computation time. Simulation results for frequency bounds are also in close agreement with analytical solutions, with the greatest discrepancies with experimental and analytical methods occurring during upward sweeps at low voltages, likely for similar reasons as for the simulation model.

Traits characteristic to the stability curve are also visible in analytical results in Fig. 10. These include the voltage necessary for starting mirror oscillations, the unstable wedge between the up-sweep and down-sweep cases, and the effect of damping to cause the wedge to round off at the bottom. The area of instability between the wedges is smallest for 30% duty cycle and progressively widens for higher duty cycles. The analytical outcomes replicate a similar trend.

It is worth discussing possible reasons that use of a linearized capacitance model during analysis appears to be generally effective at predicting stability bounds, despite

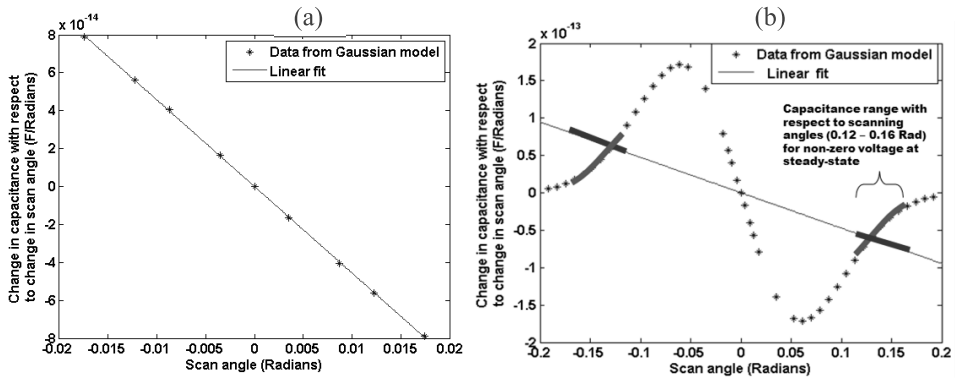

Fig. 11. Linear fit to model change in capacitance over amplitude. (a) The voltage applied was 22V for an up-sweep case at 60% duty cycle and the scanning amplitude achieved was ±1.27°. The 'a' value is −8.30E-10 and the resultant analytical voltage matches well with experimental point in stability curve. (b) The voltage applied was 60V for a down-sweep case at 50% duty cycle and the scanning amplitude achieved was ±11.01°. The 'a' value is −9.46E-11 and the capacitance highlighted between 0.12 – 0.16 Radians occurs when the voltage is switched 'ON' (non-zero voltage).

the fact that results were sensitive to the specific nonlinear capacitance model used. Fig. 11 on page 8 illustrates examples of how a varied for different ranges of scanning amplitude. For small voltages (∼20V to ∼24V) and hence small scanning amplitudes ($\theta \sim 3°$), the relationship trend between the change in capacitance and scanning amplitudes can be represented well by a linear fit.

For large voltages, averaging $dC/d\theta$ over the range of motion would appear to differ greatly from the capacitance model, but the behavior is aided by the nature of square wave excitation. During parametric resonance, non-zero voltage is applied during a finite time period at which the mirror displacement is large, as shown in Fig. 8(b). As such, the amplitude of the force applied is approximately correct with using the average slope (regions in bold), and this approximation proved sufficient for the close agreement between analytical and experimental results seen in Fig. 7.

C. Duty Cycle and Phase Trends

Driving the parametrically resonant micro-mirror results in a wedge-shaped instability region, as illustrated in Fig. 7 and known from prior works [18], [36]. The mirror does not oscillate outside the wedge and transitions sharply to large oscillatory motion inside the wedge [18], [36]. As mentioned previously, if the mirror operates at or near frequencies corresponding to maximum amplitudes, a small decrement in frequency due to potential perturbation can stop the mirror from oscillating altogether. This may necessitate future implementation of feedback control and one proposed method is to utilize the phase delay characteristics to implement phase tracking algorithms.

Fig. 12 illustrates the ability to predict phase delay trends observed from mirror simulation as a function of frequency. As excitation frequency increases, phase delay likewise increases, as would be expected from the 2nd-order structural dynamics. The minimum phase delay is observed at the frequency corresponding to maximum scanning amplitude achieved during the down-sweep motion [18]. To check phase sensitivity of the mirror to input frequency, and further verify the model in (1)-(5), a numerical simulation was performed using an Euler method to solve (1) for operation at 50% duty cycle. While not

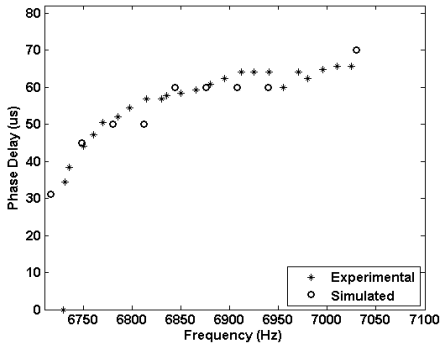

Fig. 12. Phase delay trends for 1D mirror operation at 50%. Simulation agrees with experimental outcomes within uncertainty.

all data points corresponding to experimental frequencies could be simulated due to an insufficient discretization in simulation code, the discrete levels of phase that could be obtained agree well with experimental results. In general, phase delay trends with respect to duty cycles indicate that at lower duty cycles (30% and 50%) the curves are steeper relative to curves at higher duty cycles (60% and 70%). Additionally, as duty cycles increase, the phase delay curves are shifted higher across the delay spectrum.

Additional useful trends are observed during duty cycle sweeps at fixed frequencies. Fig. 13(a) shows a series of sweeps from low to high duty cycles at 40 V for frequencies in the vicinity of the maximum scanning amplitude. While the global maximum amplitude with respect to both duty cycle and frequency at 40 V is obtained at 50% duty cycle at 6775 Hz, lower duty cycles produce maximum scanning amplitudes at lower frequencies, and higher duty cycles produce maximum scanning amplitudes at higher frequencies. These maximum amplitudes at sub-optimal frequencies are only a few percent lower than the global maximum, and importantly for practical applications, are much more robust at larger duty cycles. For instance, at 60% duty cycle there is less than 0.6° amplitude variation of 30 Hz of frequency variation, while 50% duty cycle amplitudes may vary by nearly 2° over the same range of frequencies.

Amplitude trends as a function of duty cycle can also be predicted with varying success by analytical and simulation

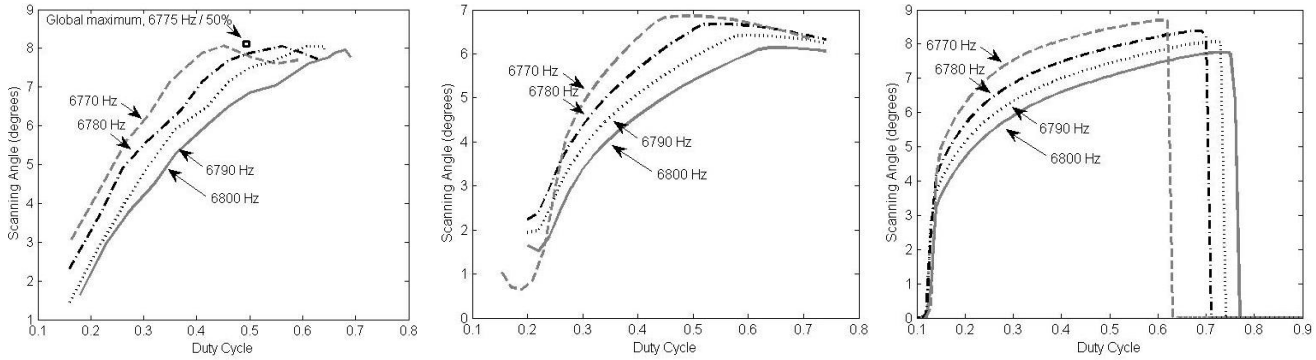

Fig. 13. (a) Experimental duty cycle sweeps at frequencies show large amplitude scanning and improved robustness against frequency variation at duty cycles exceeding 50%. (b) Analytical amplitude predictions versus duty cycle also show convergence of scanning amplitudes at elevated duty cycles, though absolute amplitude predications are less accurate. (c) Simulated response during duty cycle sweeps better predicts total amplitude, but underestimates the maximum duty cycle achieved during experimental scanning.

methods. Fig. 13(b) and Fig. 13(c) shows scanning amplitudes obtained from analytical methods and simulation, respectively. The analytical approximation for amplitude successfully captures the trend for amplitude convergence over various frequencies at elevated duty cycles, though absolute amplitude is only within about 20% of experimental results. Simulated amplitude is closer, but the convergence at high duty cycles is not well captured, largely because simulation underestimates the duty cycles that are reached with stable oscillation in experiments or analysis. This may indicate a need for finer discretization or slower adjustment from lower to higher duty cycles in the simulated response.

VI. Discussion

From the analytical and experimental behavior described above, several useful observations for duty-cycled operation of parametrically-resonant micro-mirrors can be made.

A. Ease of Implementation

The 1D micro-mirror shows both large amplitude motion and a reasonably wide range of operating frequencies under square wave excitation. This can be useful because efficiency of switched driving circuits (i.e. on-off or PWM) is typically much greater than that of analog circuits at high voltages. For instance, small capacitive loads encountered in piezoelectric micro-actuation are known to consume as much as 95% more energy in analog amplifiers than is used by the load [40], [41].

B. Open-Loop Robustness

Since in imaging applications microactuator power is not typically a dominant concern, a more important advantage of duty-cycled operation can be robustness to model error at certain duty cycles. As would be expected operating at 50% duty cycle achieves the maximum scan angle of $\pm$ 11°. However, in many applications, such as open-loop scanning for imaging, it may be more important to have a response that is robust to frequency variation than to reach the absolute maximum amplitude. However, as Fig. 13 illustrated, higher duty cycles, between about 55% and 65% for the mirror studied here, show less sensitivity (lower slope) in amplitude versus frequency,

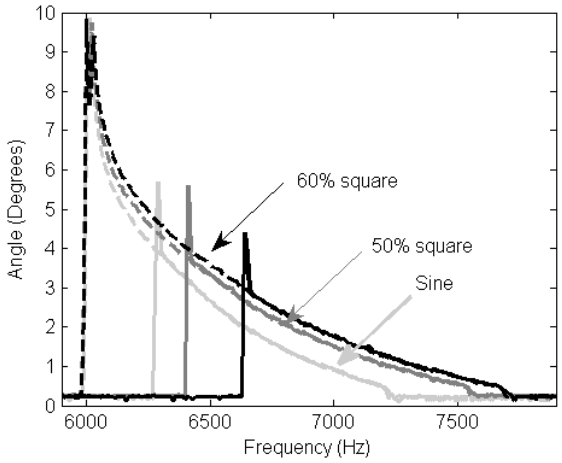

Fig. 14. Comparison of harmonic and square wave frequency sweeps at 56 V (solid: upsweep/dashed: downsweep) shows wider operating range and improve amplitude away from resonance for square wave operation. Spikes near upsweep onset are a result of incomplete transient settling during sweep.

indicating smaller amplitude changes with perturbations to the mirror's natural frequency. Furthermore, for even very small frequency offset from the optimal excitation frequency to avoid instability (on the order of 5 Hz), these duty cycles show as good or better amplitudes than a simple 50% square wave input.

As an illustration, Fig. 14 directly compares square wave and sine wave excitation for another parametrically-resonant micro-mirror of the same design. As can be seen, square wave excitation provides greater amplitudes (typically 0.5-1°) away from the maximum amplitude, and negligible loss in amplitude even at maximum. This also means slower roll-off in amplitude as frequency varies from its optimal value.

C. Control Implications

With respect to closed-loop operation, at the simplest level duty-cycled excitation provides an additional tuning parameter for amplitude adjustment when voltage and frequency are static, most likely for the benefit of simple hardware implementation. As a basic example, mirror scanning amplitude can be tuned to a fixed set point by adjusting duty cycle using a simple proportional control scheme implemented in discrete

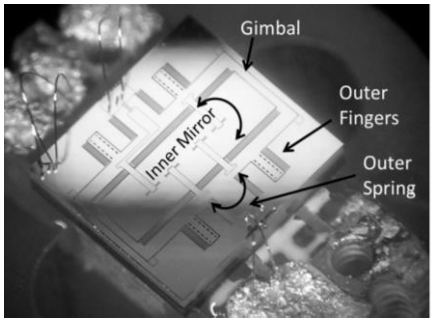

Fig. 15. Two-axis parametrically-resonant scanning mirror for dual axes confocal microscopy.

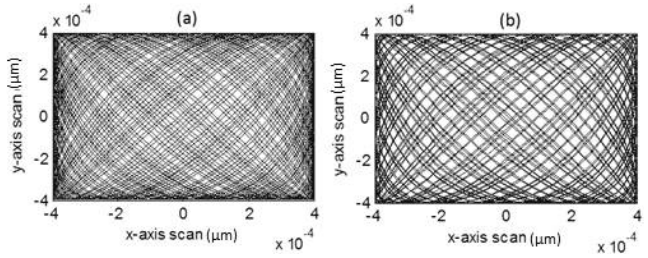

Fig. 16. Simulated image coverage of two-axis Lissajous scan (1 kHz:1.414kHz) with (a) preferred relative phase angle (b) 5% detuning of relative phase angle, shows sensitivity of image fill to scanning phase.

iterations [18]. Such a control scheme can take update in as little time as the settling time of the mirror, approximately 0.02s.

Such an approach contrasts with techniques to purely maximize amplitude, providing an alternate parameter (duty cycle) for tuning behavior and in some cases simplifying sensing as well as driving circuitry. For example, when seeking the greatest possible scanning amplitude with a square wave input, controllers for a parametrically resonant system controller would ideally turn on the input at the maximum displacement of the device within a given period, and turn off the voltage when angle returned to zero. In practice, when using on-board sensing, extremes of displacement can be difficult to measure, especially if capacitive comb fingers are also to be used for angle measurement. This is a consequence of both high resonant frequencies and large feedthrough disturbances to sensor measurements caused by large voltage changes closely timed with the critical displacement measurements used for control. Thus, in more conservative operation, some phase delay may be desirable, which can be obtained by operating at frequencies modestly higher than the critical stable frequency at the operating voltage. This allows peak amplitudes to be separated in time from driving signal, making them easier to detect in the presence of feedthrough. Once operating at a slightly sub-optimal frequency, duty cycle adjustment can be used to re-optimize amplitude, as at higher duty cycles in Fig. 12(a).

D. Multi-Axis Scanning and Future Work

A final benefit of this work is to provide methods to predict mirror response and guide mirror design and fabrication based on desired scanning specifications, including coordination of multiple axes through duty cycle tuning. While Section VI.C. discussed the use of duty cycle adjustment to optimize amplitude at a fixed frequency and voltage, to simplify driving or sensing circuit operation, it can also be useful to use duty cycle adjustments to improve coordination of scanning in multiple axes. Fig. 15 shows a modified version of the parametrically-resonant micro-mirror with two scanning axes, intended for *en face* imaging in a dual axes micro-endoscope. In experimental testing, the 2D device generally works as if it were two decoupled single-axis mirrors, though there are certain frequencies at which overlap in responses may occur.

Given a limited range of feasible resonant frequencies, such a device is operated using a Lissajous scan. Such scanning is known to have specific frequency and phase relationships that minimize the amount of time required to obtain a full image during a Lissajous scan. For example Fig. 16 shows a two axis Lissajous scan (1:1.414 frequency ratio [45]) with preferred relative phase and phase angle perturbed by 5%. As can be seen, there is a substantial difference in the amount of area covered in a finite time, and this also occurs if frequency ratio is perturbed for a given phase angle.

Availability of duty cycle as a tuning parameter, coupled with the analytical or simulation models introduced, allows scanning amplitude to be better optimized even when frequency/phase relationships are fixed between axes and voltages are constrained. Under pure sinusoidal excitation, for a single axis there are only two control parameters available, frequency and voltage, which allow only two out of three relevant scanning parameters (frequency, amplitude, and phase angle) to be adjusted independently. Once a frequency is selected in multi-axis operation, relative timing between axes is adjusted to optimize the Lissajous fill rate, and amplitude is dictated by the resulting frequency and voltage alone. When duty cycle variation is also available, even should voltage be constrained (by a maximum voltage limit or preference for equal voltage between axes), there is opportunity for further amplitude improvement, especially if the frequency relationship requires one or both axes to be places significantly above the critical frequency for that axis. As was discussed in Section VI.B. and Fig. 14, approximately 0.5-1° of amplitude increase can be obtained by replacing harmonic excitation with square wave excitation and adjusting duty cycle, even without further increasing actuation voltage. There is also some potential for use of the additional degree of freedom to avoid coupling between axes in a single multi-axis mirror with some shared electrodes, for the reasons discussed in Section VI.C.

Future work includes extending the aforementioned analytical and simulation analysis to 2D mirror designs, characterizing sources of experimental mismatch at lower voltages, and implementing phase-tracking feedback control to achieve maximum imaging rates in two-axis operation, ideally using on-chip capacitive sensing. In addition, it is desirable to extend this modeling to more general capacitance descriptions, to aid in design of mirrors with more complex geometry.

E. Disadvantages

Potential disadvantages of duty-cycled square wave excitation of a parametric scanning mirror include excitation of other

resonances and loss of torque due to voltage application only at extents of motion. Step inputs may potentially excite higher-order resonances or other overtones of the primary resonance, although this was not observed in the current experimental system. Meanwhile, applying voltage only at the extents of motion with a capacitance that is decaying with angle means that lower torques per unit voltage are being applied than at certain angles with sinusoidal excitation. However, V^2 being higher throughout the on-period of square-wave excitation helps maintain large amplitudes.

In terms of the analysis, some amount of information from non-analytical methods is required. At the very least this is damping information, while best results require some numerical fitting of the capacitance curve at large angles. However, this is a continuing obstacle for large-displacement actuator design, and analytical methods can still provide trend analysis in the absence of complete information, such as whether trade-offs in torque from placing comb fingers closer to the rotation axis (smaller moment arm, but larger capacitance over larger angles) are worthwhile.

VII. Conclusion

Simulated and analytical dynamic responses have been compared with experimental outcomes for a 1D micro-mirror for use in high resolution endoscopic imaging under parametric resonance for a range of duty cycled square wave excitations. The voltage predictions for the up-sweep and down-sweep stability bounds show good agreement with experimental observations using both analytical and simulation techniques over all duty cycles. Numerical simulations indicate reasonable agreement with experimental outcomes in amplitude estimates, particularly for high voltages (56V). Disagreements at lower voltages (32V and 40V) could perhaps be due to nonlinearities in square wave generation in the experimental system. Maximum scanning amplitudes obtained from the down-sweep case at each duty cycle and trends in phase delays for 30%, 50%, 60% and 70% duty cycle were presented. For open-loop mirror operation, when absolute maximum amplitudes are not feasible due to potential instability, this analysis indicates that a duty cycle greater than 50%, for example 60% for the sample mirror, is desirable. Larger duty cycles are found to be less sensitive to natural frequency variation, and maintain higher amplitudes as frequency increases. Duty cycle also provides an additional tuning parameter for phase or amplitude adjustment in future controller implementation using on-chip sensing.

Appendix I

To build an analytical model to determine the stability boundaries of the system at various duty cycles, the Lindstedt Poincare technique was applied to (8) to construct a relationship between δ and ε [33]. Assuming small ε, expansions of the following form were assumed:

$$\theta(\tau,\varepsilon) = \theta_0(\tau) + \varepsilon\theta_1(\tau) + \varepsilon^2\theta_2(\tau) + \cdots \tag{20}$$

$$\delta(\varepsilon) = \delta_0(\tau) + \varepsilon\delta_1(\tau) + \varepsilon^2\delta_2(\tau) + \cdots \tag{21}$$

Substituting (20) and (21) into (8) results in

$$\begin{aligned}&\left[\frac{d^2\theta_0}{d\tau^2} + \varepsilon\frac{d^2\theta_1}{d\tau^2} + \varepsilon^2\frac{d^2\theta_2}{d\tau^2} + \ldots\right]\\ &+ 2\mu\left[\frac{d\theta_0}{d\tau} + \varepsilon\frac{d\theta_1}{d\tau} + \varepsilon^2\frac{d\theta_2}{d\tau} + \cdots\right]\\ &+ [\theta_0(\tau) + \varepsilon\theta_1(\tau) + \varepsilon^2\theta_2(\tau) + \cdots]\\ &\times [\delta_0(\tau) + \varepsilon\delta_1(\tau) + \varepsilon^2\delta_2(\tau) + \cdots + \epsilon f(\tau)] = 0\end{aligned} \tag{22}$$

The damping term in (8) was then scaled to facilitate the analysis by letting $\mu = \varepsilon\hat{\mu}$ [21], [34] and this was substituted into (22). Next, coefficients of $\varepsilon^0\varepsilon^1$ (higher order terms were ignored) were equated to zero to obtain the following second order differential equations:

$$\frac{d^2\theta}{d\tau^2} + \theta_0\delta_0 = 0 \tag{23}$$

$$\frac{d^2\theta_1}{d\tau^2} + \delta_0\theta_1 = -\delta_1\theta_0 - 2\hat{\mu}\frac{d\theta_0}{d\tau} - \theta_0 f(\tau) \tag{24}$$

In order to let θ_0 be periodic with period π or 2π, the solution for (23) was assumed to be,

$$\theta_0 = a_0\cos(n\tau) + b_0\sin(n\tau) \quad \delta_0 = n^2 \tag{25}$$

where a_0 and b_0 are arbitrary constants and n is non-zero [21], [26], [33].

Substituting (23) into (24) yields

$$\begin{aligned}\frac{d^2\theta_1}{d\tau^2} + \delta_0\theta_1 = &-\delta_1(a_0\cos(n\tau) + b_0\sin(n\tau) - 2\hat{\mu}(b_0 n\cos(n\tau)\\ &- a_0 n\sin(n\tau)) - f(\tau)(a_0\cos(n\tau) + b_0\sin(n\tau))\end{aligned} \tag{26}$$

For θ_1 to be periodic, the secular terms $(\cos(n\tau), \sin(n\tau))$ on the right hand side of (26) are eliminated [21], [26] and this results in

$$[\delta_1 + \frac{1}{2}\alpha_m]a_0 + \left[\frac{1}{2}\beta_m + 2\hat{\mu}n\right]b_0 = 0 \tag{27}$$

$$\left[\frac{1}{2}\beta_m - 2\hat{\mu}n\right]a_0 + [\delta_1 - \frac{1}{2}\alpha_m]b_0 = 0 \tag{28}$$

For a non-trivial solution to exist,

$$\delta_1^2 = \frac{1}{4}\left(\beta_m^2 + \alpha_m^2\right) - 4\hat{\mu}^2 n^2 \tag{29}$$

$$\delta_1 = \pm\sqrt{\frac{\left(\beta_m^2 + \alpha_m^2\right)}{4} - \frac{4n^2\mu^2}{\varepsilon^2}} \tag{30}$$

Substituting δ_1 and δ_0 into (21) results in (11) in Section III.

References

[1] M. Faraday, "On a peculiar class of acoustical figures and on certain forms assumed by a group of particles upon vibrating elastic surfaces," *Phil. Trans. Roy. Soc. London*, vol. 121, pp. 299–340, Jan. 1831.

[2] T. I. Fossen and H. Nijmeijer, "Detection of parametric roll for ships," in *Parametric Resonance in Dynamical Systems*. New York, NY, USA: Springer, 2012, pp. 17–43.

[3] Y. S. Shin, V. L. Belenky, J. R. Paulling, K. M. Weems, and W. M. Lin, "Criteria for parametric roll of large containerships in longitudinal seas," *Trans. SNAME*, vol. 112, pp. 14–47, Jan. 2004.

[4] S. M. Carmel, "Study of parametric rolling event on a panamax container vessel," *J. Transp. Res. Board*, vol. 1643, no. 1, pp. 56–63, 2006.

[5] N. Umeda, H. Hashimoto, S. Minegaki, and A. Matsuda, "An investigation of different methods for the prevention of parametric rolling," *J. Marine Sci. Technol.*, vol. 13, no. 1, pp. 16–23, 2008.
[6] I. G. Raftoyiannis, "Parametric resonance of steel bridges pylons due to periodic traffic loads," *Archive Appl. Mech.*, vol. 82, nos. 10–11, pp. 1601–1611, 2012.
[7] G. F. Royer-Carfagni, "Parametric-resonance-induced cable vibrations in network cable-stayed bridges. A continuum approach," *J. Sound Vibrat.*, vol. 262, no. 5, pp. 1191–1222, 2003.
[8] N. I. Markevich and E. E. Sel'kov, "Parametric resonance and amplification in excitable membranes. The Hodgkin–Huxley model," *J. Theoretical Biol.*, vol. 140, no. 1, pp. 27–38, 1989.
[9] M. V. Requa and K. L. Turner, "Electromechanically driven and sensed parametric resonance in silicon microcantilevers," *Appl. Phys. Lett.*, vol. 88, no. 26, pp. 263508-1–263508-3, 2006.
[10] B. J. Gallacher, J. S. Burdess, and K. M. Harish, "A novel excitation scheme for MEMS gyroscopes using parametric pumping for near inertial grade performance," *Proc. SPIE*, vol. 6113, p. 611305, Jan. 2006.
[11] D. W. Carr, S. Evoy, L. Sekaric, H. G. Craighead, and J. M. Parpia, "Parametric amplification in a torsional microresonator," *Appl. Phys. Lett.*, vol. 77, no. 10, pp. 1545–1547, Sep. 2000.
[12] J. F. Rhoads, S. W. Shaw, K. L. Turner, and R. Baskaran, "Tunable micromechanical filters that exploit parametric resonance," *J. Vibrat. Acoust.*, vol. 127, no. 5, pp. 423–430, Oct. 2005.
[13] A. Arslan, D. Brown, W. O. Davis, S. Holmstrom, S. K. Gokce, and H. Urey, "Comb-actuated resonant torsional microscanner with mechanical amplification," *J. Microelectromech. Syst.*, vol. 19, no. 4, pp. 936–943, Aug. 2010.
[14] C. Qian, J. Murphy-Boesch, S. Dodd, and A. Koretsky, "Sensitivity enhancement of remotely coupled NMR detectors using wirelessly powered parametric amplification," *Magn. Reson. Med.*, vol. 68, no. 3, pp. 989–996, Sep. 2012.
[15] D. L. Dickensheets and G. S. Kino, "Silicon-micromachined scanning confocal optical microscope," *J. Microelectromech. Syst.*, vol. 7, no. 1, pp. 38–47, Mar. 1998.
[16] H. Ra, W. Piyawattanametha, Y. Taguchi, D. Lee, M. J. Mandella, and O. Solgaard, "Two-dimensional MEMS scanner for dual-axes confocal microscopy," *J. Microelectromech. Syst.*, vol. 16, no. 4, pp. 969–976, 2007.
[17] J. T. C. Liu *et al.*, "Micromirror-scanned dual-axis confocal microscope utilizing a gradient-index relay lens for image guidance during brain surgery," *J. Biomed. Opt.*, vol. 15, no. 2, pp. 026029-1–026029-5, Apr. 2010.
[18] W. Shahid, Z. Qiu, X. Duan, H. Li, T. D. Wang, and K. R. Oldham, "Modeling and simulation of a parametrically excited micro-mirror with duty-cycled square-wave excitation," in *Proc. ASME Int. Des. Eng. Tech. Conf., Comput. Inf. Eng. Conf.*, 2013.
[19] Z. Qiu *et al.*, "Targeted vertical cross-sectional imaging with handheld near-infrared dual axes confocal fluorescence endomicroscope," *Biomed. Opt. Exp.*, vol. 4, no. 2, pp. 322–330, Feb. 2013.
[20] K. L. Turner, S. A. Miller, P. G. Hartwell, N. C. Macdonald, S. H. Strogartz, and S. G. Adams, "Five parametric resonances in a microelectromechanical system," *Lett. Nature*, vol. 396, no. 6707, pp. 149–152, 1998.
[21] A. H. Nayfeh and D. T. Mook, *Nonlinear Oscillations*. Hoboken, NJ, USA: Wiley, 1979, pp. 258–364.
[22] W. Shahid, Z. Qiu, X. Duan, H. Li, T. D. Wang, and K. R. Oldham, "Modeling, testing and control of a parametrically excited micro-mirror with duty-cycled excitation," in *Proc. Amer. Control Conf.*, Washington, DC, USA, Jun. 2013, pp. 17–19.
[23] W. Magnus and S. Winkler, "Basic concepts," in *Hill's Equation*. Hoboken, NJ, USA: Wiley, 1966, pp. 3–10.
[24] C. Cattani, E. A. Grebenikov, and A. N. Prokopenya, "On stability of the Hill equation with damping," *Nonlinear Oscillations*, vol. 7, no. 2, pp. 168–178, 2004.
[25] E. Butikov, "Parametric resonance in a linear oscillator at square-wave modulation," *Eur. J. Phys.*, vol. 26, no. 1, pp. 157–174, 2005.
[26] A. H. Nayfeh, "Characteristic exponents and stability of Hill's equation," *J. Appl. Mech.*, vol. 39, no. 4, pp. 1156–1158, 1972.
[27] A. P. Seyranian, "Theory of parametric resonance: Modern results," in *Proc. Int. Conf. Phys. Control*, vol. 4. Aug. 2003, pp. 1052–1060.
[28] C. Ataman and H. Urey, "Modeling and characterization of comb-actuated resonant microscanners," *J. Micromech. Microeng.*, vol. 16, no. 1, pp. 9–16, Jan. 2006.
[29] S. Maruyama, M. Nakada, M. Mita, T. Takahashi, H. Fujita, and H. Toshiyoshi, "An equivalent circuit model for vertical comb drive MEMS optical scanner controlled by pulse width modulation," *IEEJ Trans. Sensors Micromach.*, vol. 132, no. 1, pp. 1–9, Jun. 2011.
[30] W. Zhang, R. Baskaran, and K. L. Turner, "Effect of cubic nonlinearity on auto-parametrically amplified resonant MEMS mass sensor," *Sens. Actuators A, Phys.*, vol. 102, no. 1, pp. 139–150, 2002.
[31] K. L. Turner, P. G. Hartwell, F. M. Bertsch, and N. C. MacDonald, "Parametric resonance in a microelectromechanical torsional oscillator," in *Proc. ASME Int. Mech. Eng. Congr. Exposit. MEMS*, Anaheim, CA, USA, Nov. 1998, pp. 335–340.
[32] C. Ataman and H. Urey, "Nonlinear frequency response of comb-driven microscanners," *Proc. SPIE*, vol. 5348, pp. 166–174, Jan. 2004.
[33] A. H. Nayfeh, *Introduction to Perturbation Techniques*. Hoboken, NJ, USA: Wiley, 1981, pp. 134–143.
[34] R. H. Rand. (2000). *Lecture Notes on Nonlinear Vibrations, Version 34a* [Online]. Available: http://www.tam.cornell.edu/randdocs/
[35] J. Korvink and O. Paul, "Free space optical MEMS," in *MEMS: A Practical Guide to Design, Analysis and Applications*. New York, NY, USA: William Andrew Inc., 2006, pp. 356–361.
[36] B. E. DeMartini, J. F. Rhoads, K. L. Turner, S. W. Shaw, and J. Moehlis, "Linear and nonlinear tuning of parametrically excited MEMS oscillators," *J. Microelectromech. Syst.*, vol. 16, no. 2, pp. 310–318, Apr. 2007.
[37] W. Piyawattanametha *et al.*, "In vivo near-infrared dual-axis confocal microendoscopy in the human lower gastrointestinal tract," *J. Biomed. Opt.*, vol. 17, no. 2, pp. 0211021–0211024, Feb. 2012.
[38] J. F. Rhoads, S. W. Shaw, K. L. Turner, J. Moehlis, B. E. DeMartinin, and W. Zhang, "Generalized parametric resonance in electrostatically actuated microelectromechanical oscillators," *J. Sound Vibrat.*, vol. 296, nos. 4–5, pp. 797–829, Oct. 2006.
[39] Y. Linzon, B. Ilic, S. Lulinsky, and S. Krylov, "Efficient parametric excitation of silicon-on-insulator microcantilever beams by fringing electrostatic fields," *J. Appl. Phys.*, vol. 113, no. 16, pp. 163508-1–163508-11, 2013.
[40] D. V. Newton, L. Massengill, and E. Garcia, "Efficient power amplifiers for piezoelectric applications," *Smart Mater. Struct.*, vol. 5, no. 6, pp. 766–775, 1996.
[41] B. Edamana, B. Hahn, J. S. Pulskamp, R. G. Polcawich, and K. R. Oldham, "Modeling and optimal low-power on-off control of thin-film piezoelectric rotational actuators," *IEEE/ASME Trans. Mechatronics*, vol. 16, no. 5, pp. 884–896, Oct. 2011.
[42] H. Schenk *et al.*, "Large deflection micromechanical scanning mirrors for linear scans and pattern generation," *IEEE J. Sel. Topics Quantum Electron.*, vol. 6, no. 5, pp. 715–722, Oct. 2000.
[43] H. Li, Z. Qiu, X. Duan, K. R. Oldham, K. Kurabayashi, and T. D. Wang, "2D resonant microscanner for dual axes confocal fluorescence endomicroscope," in *Proc. IEEE 27th Int. Conf. MEMS*, Jan. 2014, pp. 805–808.
[44] Z. Qiu *et al.*, "Vertical cross-sectional imaging of colonic dysplasia in vivo with multi-spectral dual axes confocal endomicroscopy," *Gastroenterology*, vol. 146, no. 3, pp. 615–617, 2014.
[45] A. Kovacs, "Scanning strategies for imaging arrays," *Proc. SPIE*, vol. 7020, p. 702007, Aug. 2008

Wajiha Shahid received the B.S. in Mechanical Engineering from the University of Michigan in 2009, and the M.S. in Mechanical Engineering from the University of Michigan in 2012. Her research interests include nonlinear dynamics and simulation and control of nonlinear systems.

Zhen Qiu received the Bachelor degree in Mechanical Engineering from Department of Precision Instruments and Mechanology, Tsinghua University, Beijing, China, and the Ph.D. degree in Biomedical Engineering from the University of Michigan, Ann Arbor, MI, USA, in 2013. His current research interests include MEMS devices based medical endomicroscope development and bio-optical imaging.

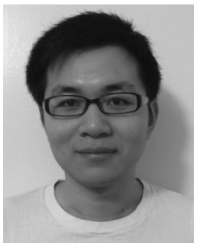

Xiyu Duan was born in Jiangxi, China. He received the B.S. in Electrical Engineering from the Hong Kong University of Science and Technology, and the M.S. degree in Electrical Engineering from the University of Michigan. Since 2012, he has been pursuing the Ph.D. degree in Biomedical Engineering in the University of Michigan. His research focus is building miniature confocal and multiphoton imaging instruments using MEMS devices.

Haijun Li received the Ph.D. degree in in microelectronics and solid state electronics from Jilin University, Changchun,China, in 2007.

He is currently a Research Fellow in University of Michigan, Ann Arbor, Michigan, USA, and working on the development of MEMS-based microendoscope. Before joining this project, he held a Postdoctoral position at Nanyang Technology University, Singapore (2008-2011), and was a Senior Engineer at Hebei Semiconductor Research Institute, Shijiazhuang, China (1997–2008). His research interests include MEMS, uncooled Infrared detectors, epi-MEMS technology, and wafer level packaging technologies.

Thomas D. Wang received his B.S. degree from Harvey Mudd College in 1985 and Ph.D. degree in biomedical engineering from MIT in 1996. He was a Postdoctoral Fellow at the Wellman Laboratory of Photomedicine from 1996 to 1998. He is currently an Associate Professor of Medicine, Biomedical Engineering, and Mechanical Engineering at the University of Michigan. His research interests are in the field of biomedical optics and the use of MEMS to perform scanning and actuation.

Kenn R. Oldham is an Associate Professor of Mechanical Engineering at the University of Michigan. Prof. Oldham received the Ph.D. in Mechanical Engineering from the University of California at Berkeley in 2006 and the B.S. in Mechanical Engineering from Carnegie Mellon University in 2000. He joined the University of Michigan in 2007 following a post-doctoral fellowship at the Army Research Laboratory. Prof. Oldham and his research group study the intersection of control systems and micro-scale sensing and actuation, with interests in design for controllability, optimal and robust control, and novel sensor and actuator design. Applications of this research include terrestrial micro-robotics, endoscopic microscopy, and inertial and physiological sensing.